applied sciences

MDPI

Article

Hydrodynamic and Morphological Effects of Non-Powered Floating Objects on Sediment Resuspension: A CFD and Regression Analysis

Nuray Gedik [1], Onur Bora [2,*], Mehmet Sedat Kabdaşlı [3] and Emel İrtem [4]

[1] Department of Civil Engineering, Balikesir University, Balikesir 10145, Türkiye; ngedik@balikesir.edu.tr
[2] Department of Science Affairs, Balikesir Metropolitan Municipality, Balikesir 10185, Türkiye
[3] Formerly at the Faculty of Civil Engineering, Istanbul Technical University, Istanbul 34672, Türkiye; kabdaslim@gmail.com
[4] Department of Civil Engineering, Doğuş University, Istanbul 34775, Türkiye; eirtem@dogus.edu.tr
* Correspondence: bora.onur@gmail.com; Tel.: +90-505-700-8321

Abstract: This study investigates the hydrodynamic and morphological effects caused by non-powered floating objects (e.g., barges, pontoons, and floating or moored platforms) that are towed by external forces (such as tugboats) across flat, shallow seabeds. This study employs an integrated approach combining advanced computational fluid dynamics (CFD) simulations with multivariate polynomial regression analysis to systematically investigate the hydrodynamic and morphological effects of non-powered floating objects on sediment resuspension. A total of 96 simulation scenarios were conducted, of which 84 significant cases (where the floating object did not touch the seabed) were analyzed. Variations included bow geometries (blunt and raked), towing speeds, and operational parameters. The results indicate that, under similar towing speeds and clearance heights, blunt bows increase the suspended sediment concentration by approximately 90–190% compared to raked bows. The regression model, attaining an R-squared value of 0.9647, identified the Froude number, squat ratio, squared towing time, and object type as critical predictors of suspended sediment concentration. Furthermore, the interaction terms between the Froude number and object type were significant, enhancing the model's predictive accuracy. These results underscore the importance of optimized design and operational strategies in minimizing the environmental impact of floating structures, especially in shallow marine environments where sediment dynamics play a crucial role in ecological balance. Careful consideration of towing speed, object geometry, and operational parameters can significantly reduce sediment resuspension, mitigating ecological consequences.

Keywords: computational fluid dynamics (CFD); hydrodynamic; non-powered floating objects; sediment resuspension

check for updates

Academic Editor: Francesca Scargiali

Received: 21 January 2025
Revised: 26 February 2025
Accepted: 28 February 2025
Published: 4 March 2025

Citation: Gedik, N.; Bora, O.; Kabdaşlı, M.S.; İrtem, E. Hydrodynamic and Morphological Effects of Non-Powered Floating Objects on Sediment Resuspension: A CFD and Regression Analysis. *Appl. Sci.* **2025**, *15*, 2717. https://doi.org/10.3390/app15052717

Copyright: © 2025 by the authors. Licensee MDPI, Basel, Switzerland. This article is an open access article distributed under the terms and conditions of the Creative Commons Attribution (CC BY) license (https://creativecommons.org/licenses/by/4.0/).

1. Introduction

Sediment resuspension is a critical issue in coastal and shallow water environments, where it can lead to significant ecological and environmental impacts, including habitat loss, decreased water quality, and the alteration of benthic ecosystems. These effects are particularly pronounced in sensitive coastal regions, where natural sediment stability is already compromised by anthropogenic pressures such as dredging, coastal construction, and the operation of heavy maritime traffic. Although extensive research has focused on sediment dynamics influenced by natural forces and powered vessels—where propeller

wash and engine thrust create complex flow fields—the hydrodynamic and morphological effects of non-powered floating objects remain largely uncharted. Unlike their powered counterparts, non-powered objects (e.g., barges, pontoons, and moored platforms) rely solely on external towing forces. This results in distinct pressure fields, wake patterns, and flow regimes that lead to different sediment mobilization characteristics, especially under shallow water conditions. Addressing this gap is essential for developing design and operational strategies that minimize environmental impacts in coastal regions.

Non-powered floating objects, such as barges, pontoons, and floating platforms commonly used in industrial and maritime operations, are typically towed or moored in shallow marine environments characterized by flat or nearly flat seabeds. These objects, unlike powered vessels, lack propulsion systems and rely on external forces for movement, making their hydrodynamic interactions with the seabed distinct from those of self-propelled vessels. The study focuses on objects towed at subcritical Froude numbers (Fr < 1) over a flat, sandy bed (d_{50} = 0.0625 mm) in shallow water conditions, representing common operational scenarios in coastal environments.

Numerous studies have examined the various parameters that influence suspended sediment concentrations in marine environments, including waves, currents, wind, and water depth. However, research focusing specifically on the hydromorphological effects caused by floating objects is relatively limited. For example, Ravens [1] highlighted the role of high-frequency ship waves (T~6 s) in sediment transport in Boston Harbor, particularly in Dorchester Bay, even in the absence of storm conditions.

Maynord [2] studied the physical forces exerted by ships to determine ship-induced sediment transport and suspended sediment concentrations. Parchure et al. [3] proposed a method for calculating suspended sediment amounts for cohesive and non-cohesive sediments under the influence of ship-generated waves, using simple mathematical expressions and approaches. This simplified method allows for preliminary predictions of suspended sediment concentrations.

The relationship between boat wakes and sediment resuspension was also explored by Bauer et al. [4], who noted a strong correlation between boat-generated waves and levee erosion in the Sacramento-San Joaquin Delta. McConchie and Toleman [5] further demonstrated that boat-induced suspended sediment concentrations could be up to 80-times greater than those caused by wind-generated waves, particularly in river environments with limited fetch lengths. Similarly, Houser [6] showed that in narrow channels like rivers, hydrodynamic effects caused by ships have a greater impact on suspended sediment concentrations than wind-generated waves.

The environmental consequences of these hydrodynamic disturbances have been observed in various ecosystems. Eriksson et al. [7] studied the effects of boating activities on aquatic vegetation in the Stockholm archipelago of the Baltic Sea. Their research at 44 different sites demonstrated that morphological effects caused by leisure boats or medium-sized vessels could significantly alter community diversity, negatively impacting species richness and the development of aquatic vegetation in deeper waters. Further emphasizing the environmental consequences, Rapaglia et al. [8] found that in the Venice Lagoon, heavy ship traffic increased sediment suspension times up to one hour, despite typically short suspension durations in such environments. This prolonged suspension can have detrimental effects on water quality and aquatic life, indicating the broader ecological implications of vessel-induced sediment resuspension.

Zaggia et al. [9] investigated shoreline changes in the Malamocco–Marghera Canal in the Venice Lagoon, based on field measurements and satellite imagery analyses. They determined that one of the most significant causes of erosion along the shoreline was the hydrodynamic effects generated by heavy ship traffic, leading to an annual shoreline retreat of 3–4 m. Duro

et al. [10] extensively examined the effects of vessels on riverbanks and protections, as well as shoreline changes in the Meuse River in the Netherlands. Using advanced measurement techniques, they provided detailed insights into how vessel-induced hydrodynamic forces contribute to bank erosion and morphological alterations. Mao and Chen [11] conducted field measurements in the Grand Canal, a heavily trafficked waterway in China's Jiangsu region, analyzing ship-induced wave and current data. Their findings highlighted that bed flow velocities increased significantly due to ship traffic, with single ship passages increasing bed flow velocity up to nine times compared to conditions without ship passage.

To address the gaps in understanding the complex interactions between floating objects and sediment dynamics, some studies have employed advanced modeling and experimental techniques. For example, Ji et al. [12,13] utilized three-dimensional numerical models to examine suspended sediment concentrations resulting from hydrodynamic effects caused by ships with and without propellers. Their work provided insights into the compounding effects of ship-generated waves and propeller action on sediment resuspension in confined shipping channels. Du et al. [14] performed experimental towing tests and numerical modeling using inland water convoys, analyzing the influence of channel width, water depth, and ship draft on ship resistance and sediment movement. Their analyses showed that smaller channel widths, shallower water depths, and greater ship drafts significantly increased ship resistance, which can, in turn, affect sediment resuspension patterns.

Physical modeling studies have also contributed to this understanding. Robijns [15] conducted physical model tests to investigate the forces on ships and the flow velocities and pressures on the seabed during ship movement. The experiments revealed that the most critical parameters affecting flow velocities under the ship were the shape of the ship's bow and the clearance between the ship and the seabed. Similarly, Schroevers et al. [16] carried out full-scale physical experiments using a deeply loaded barge in the Juliana Canal in the Netherlands. They observed significant erosion in the canal bed, with gravel in the middle of the canal moving towards the sides after each passage, highlighting the impact of vessel movement on bed stability.

The reviewed literature predominantly focuses on powered vessels, where propeller-induced turbulence and engine thrust dominate the sediment transport mechanisms. Non-powered floating objects, however, represent a distinctly different case where pressure gradients, wake patterns, and flow regimes arise solely from object geometry and movement characteristics. This fundamental difference in hydrodynamic mechanisms necessitates dedicated investigation, as existing theoretical frameworks developed for powered vessels cannot be directly applied.

The preceding review demonstrates that while vessel-induced sediment dynamics have been extensively studied, the unique interactions between geometric parameters (bow shape, width, length) and operational conditions (towing speed, clearance height) in non-powered objects create distinct flow patterns and sediment transport mechanisms that require systematic investigation. Additionally, the combined effects of design features and operational parameters on sediment dynamics need to be quantified for effective environmental impact mitigation. To address these knowledge gaps, this study employs advanced computational fluid dynamics (CFD) simulations coupled with multivariate regression analysis. Through systematic variation in geometric and operational parameters, the investigation aims to elucidate the complex interactions governing sediment resuspension beneath non-powered floating objects.

Therefore, the primary objectives of this study are as follows:

1. Investigate the hydrodynamic effects induced by non-powered floating objects with varying geometries (blunt and raked bows) and dimensions when towed over flat seabeds.

2. Quantify the resultant sediment resuspension and morphological changes on the seabed under different operational parameters, including towing speeds and clearance heights.
3. Develop a predictive multivariate regression model that captures the relationships between object geometry, operational parameters, and sediment resuspension, thereby providing a tool for designing environmentally sustainable floating structures.

To achieve these objectives, 96 CFD simulation scenarios were conducted using FLOW-3D Hydro V1.0 software, systematically varying key parameters to capture a comprehensive range of conditions. The simulations were complemented by a multivariate polynomial regression analysis to identify the most significant predictors of sediment resuspension and to develop a robust predictive model.

2. Materials and Methods

An integrated methodology is employed in this study, comprising two complementary components. First, advanced three-dimensional CFD simulations are used to model the complex fluid–sediment interactions under a range of operational parameters. Second, a robust multivariate polynomial regression analysis is conducted to systematically quantify the influence of these parameters on sediment resuspension.

FLOW-3D Hydro software was used in this analysis to build a 3D hydro-morphodynamic numerical model. Flow Science, Inc. created FLOW-3D Hydro, a commercial software kit. Flow-3D uses a finite volume approach to solve the continuity equation (Equation (1)) and the unsteady Reynolds-averaged Navier–Stokes equations governing fluid motion (Equation (2)) [17].

$$\frac{\partial}{\partial X_i} U_i A_i = 0 \tag{1}$$

$$\frac{\partial U_i}{\partial t} + \frac{1}{V_f}\left(U_j A_j \frac{\partial u}{\partial X_j}\right) = -\frac{1}{\rho}\frac{\partial P}{\partial X_i} + G_i + f_i \tag{2}$$

$$\rho V_f f_i = \tau_{b,i} - \left[\frac{\partial}{\partial X_j}(A_j S_{ij})\right]; S_{ii} = -2\mu_{tot}\left[\frac{\partial U_i}{\partial X_i}\right]; S_{ij} = -\mu_{tot}\left[\frac{\partial U_i}{\partial X_j} + \frac{\partial U_j}{\partial X_i}\right] \tag{3}$$

where P indicates pressure, U_i is the mean velocity, time is denoted by t, A_i is the fractional open area open to flow in the i direction, V_f is the fractional volume open to flow, G_i represents the body accelerations, f_i indicates the viscous accelerations, S_{ij} is the strain rate tensor, $\tau_{b,i}$ denotes the wall shear stress, ρ is the density of water, μ_{tot} is the total dynamic viscosity, which includes the effects of turbulence ($\mu_{tot} = \mu + \mu_T$), μ is the dynamic viscosity, and μ_T is the eddy viscosity.

Sediment transport modeling requires accurate estimates of the near-wall shear stresses, so a good turbulence model should be selected for turbulence flows. In FLOW-3D, there are six turbulence models available: the Prandtl mixing length model, the one-equation, the two-equation k-ε, RNG, and k-ω models, and a large eddy simulation, LES, model. The Renormalization Group (RNG) turbulence model [18] is used in this study. The RNG model uses equations similar to the equations for the k-ε model. However, equation constants that are found empirically in the standard k-ε model are derived explicitly in the RNG model. In particular, the RNG model is known to describe low-intensity turbulence flows and flows having strong shear regions more accurately. RNG turbulence model equations are shown below.

$$\frac{\partial(\rho k)}{\partial t} + \frac{\partial(\rho k u_i)}{\partial x_i} = \frac{\partial}{\partial x_j}\left[\left(\mu + \frac{\mu_t}{\sigma_k}\right)\frac{\partial k}{\partial x_j}\right] + P_k - \rho\varepsilon \tag{4}$$

$$\frac{\partial(\rho\varepsilon)}{\partial t} + \frac{\partial(\rho\varepsilon u_i)}{\partial x_i} = \frac{\partial}{\partial x_j}\left[\left(\mu + \frac{\mu_t}{\sigma_\varepsilon}\right)\frac{\partial(\varepsilon)}{\partial x_j}\right] + C_{1\varepsilon}\frac{\varepsilon}{k}P_k - C_{2\varepsilon}\rho\frac{\varepsilon^2}{k} \tag{5}$$

where k is the turbulence kinetic energy (henceforth, TKE), ε is the dissipation rate, ρ is density, t is time, x_i is the coordinate in the (i) axis, μ is the dynamic viscosity, μ_t is the turbulent dynamic viscosity, and P_k is the production of TKE. The default values of $C_{1\varepsilon}$, $C_{2\varepsilon}$, and $\sigma_k = \sigma_\varepsilon$ are 1.42, 1.68, and 1.39, respectively. The turbulent viscosity is computed using the parameter $C_\mu = 0.85$ using Equation (6).

$$\mu_T = \rho C_\mu \frac{k^2}{\epsilon} \tag{6}$$

Sediment is entrained by picking-up and resuspension due to shearing and small eddies at the packed sediment interface. Because it is not possible to compute the flow dynamics about each individual grain of sediment, an empirical model must be used. The model used here is based on Mastbergen and Van den Berg. The first step to computing the critical Shields parameter is calculating the dimensionless parameter $d_{*,i}$:

$$d_{*,i} = d_i \left[\frac{\rho_f \left(\rho_i - \rho_f \right) \|g\|}{\mu_f^2} \right]^{1/3} \tag{7}$$

where ρ_i is the density of the sediment species I, ρ_f is the fluid density, d_i is the diameter, μ_f is the dynamic viscosity of fluid, and $\|g\|$ is the magnitude if the acceleration of gravity g.

From this, the dimensionless critical Shields parameter is computed using the Soulsby–Whitehouse equation:

$$\theta_{cr,i} = \frac{0.3}{1 + 1.2 d_{*,i}} + 0.055[1 - \exp(-0.02 d_{*,i})] \tag{8}$$

The critical Shields parameter can be modified for sloping surfaces to include the angle of repose. The modification further alters $\theta_{cr,i}$

$$\theta'_{cr,i} = \theta_{cr,i} \frac{\cos\psi \sin\beta + \sqrt{\cos^2\beta \tan^2\ \varphi_i - \sin^2\psi \sin^2\beta}}{\tan\ \varphi_i} \tag{9}$$

where β is the angle of slope of bed, φ is the user-defined angle of repose for sediment species i (default is 32), and ψ is the angle between the flow and the upslope direction [17].

The local Shields parameter is computed based on the local bed shear stress, τ:

$$\theta_i = \frac{\tau}{\|g\| d_i \left(\rho_i - \rho_f \right)} \tag{10}$$

where τ is calculated using the law of the wall for 3D turbulent flow and the quadratic law of bottom shear stress for shallow-water turbulent flow, respectively, with consideration of the bed surface roughness. The settling velocity equation proposed by Soulsby [19] is used:

$$u_{settling,i} = \left[\left(10.36^2 + 1.049 d_*^3 \right)^{0.5} - 10.36 \right] \tag{11}$$

Bed-load transport is a mode of sediment transport caused by rolling or bouncing over the surface of the packed bed of sediment. The volumetric transport rate of sediment per width of bed is as follows [20]:

$$\Phi_i = \beta_{VT,i} d_{*,i}^{-0.3} \left(\frac{\theta_i}{\theta'_{cr,i}} - 1.0 \right)^{2.1} c_{b,i} \tag{12}$$

where the $\beta_{VT,i}$ coefficient is 0.053. $c_{b,i}$ is the volume fraction of species i in the bed material.

For each species, the suspended sediment concentration is calculated by solving its own transport equation,

$$\frac{\partial C_{s,i}}{\partial t} + \nabla.(u_{s,i} C_{s,i}) = \nabla.\nabla(D C_{s,i}) \tag{13}$$

Here, $C_{s,i}$ is the suspended sediment mass concentration of species i, which is defined as the sediment mass per volume of fluid-sediment mixture; D is the diffusivity; and $u_{s,i}$ is the suspended sediment velocity.

The FAVOR (Fractional Area/Volume Obstacle Representation) method for the description of the geometry and the Volume-of-Fluid (VOF) method as originally described by Hirt and Nichols [21] for tracking fluid interfaces are used in the model. Typically, the fractional volume is represented by the quantity. In interior regions of liquid, the value of F would be 1.0, while outside of the liquid, in regions of gas (air, for example), the value of F is zero. The location of a free surface is where F changes from 0.0 to 1.0. Thus, any element having an F value lying between 0.0 and 1.0 must contain a surface. In addition, the normal to the surface can be calculated from the direction in which F changes most rapidly, applying boundary conditions to the surface.

$$\frac{\partial F}{\partial t} + \frac{\partial F}{\partial t} + \frac{1}{V_f}\left[A_X u \frac{\partial F}{\partial X} + A_y v \frac{\partial F}{\partial Y} + A_z w \frac{\partial F}{\partial z}\right] = 0 \quad (14)$$

In the FAVOR method, a geometric surface can cut through a rectangular mesh cell, dividing it into blocked and open portions. The ratio of the open volume in a cell to its total volume is called the fractional volume. The intersections of the surface with the faces of the cell (six in three dimensions) are computed and stored as fractional areas, which are the ratios of the open area to the total area at the respective cell face.

In Flow-3D software, the determination of free surfaces with the water–air interface is carried out by the VOF method depending on whether the cells are completely filled with water, empty, or partially filled. In this method, a value of 1 represents the cell when it is completely filled with fluid, 0 when it is completely empty, and therefore the free surface when it is between 0 and 1.

3. Model Simulation Setup

To determine the dimensions of the floating object, a market survey was conducted, analyzing 40 different barges (floating object) to extract ratios of length/depth, width/depth, and length/width. Based on the obtained ratios, two different floating objects with lengths of 15 m, widths of 6 m, and depths of 2 m were selected—one with a blunt bow and the other with a raked bow. The dimensions of the floating object were varied in relevant scenarios. Figure 1 illustrates the floating object with a blunt bow, while Figure 2 shows the floating object with a raked bow.

The dimensions of the computational domain were chosen to encompass the time interval necessary to observe the hydrodynamic and morphodynamic features examined in this study. Additionally, the study area for the parameters of interest needed to be sufficiently distant from the domain boundaries to avoid potential influences from boundary conditions. The maximum towing speed of the floating object was considered as 2 m/s in this study. The object accelerates to this speed in 25 s and continues to be towed at this speed for an additional 25 s. Considering the total distance covered by the floating object, the length of the computational domain was set to 100 m.

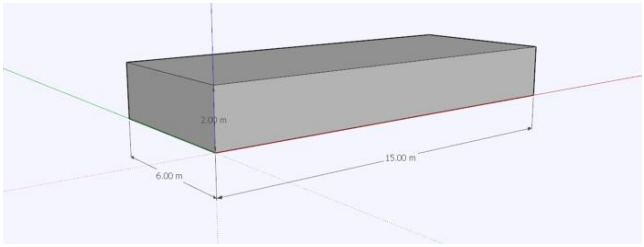

Figure 1. Isometric view of Floating Object 1 with a blunt bow.

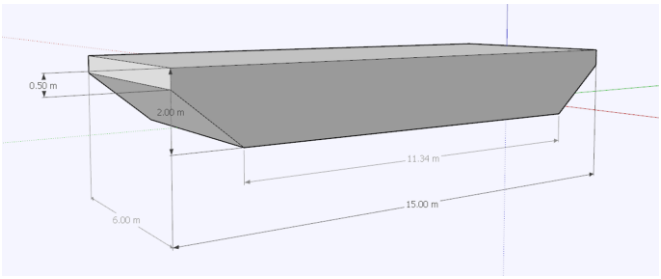

Figure 2. Isometric view of Floating Object 2 with a raked bow.

To determine the width of the computational domain, various numerical models were created to examine the effects of domain width on the hydrodynamic and morphodynamic results. Based on these analyses, the domain width was set to 28 m to ensure that the movements of the floating object and the resulting morphological changes on the seabed were not affected by the boundaries.

The determination of grid size is crucial to accurately represent the physics of interest while maintaining computational efficiency. A sensitivity analysis was performed to optimize the grid size and structure. The analysis began with an initial grid configuration suitable for the physics to be examined, followed by systematic reductions in grid size. Hydrodynamic results, morphological changes, and computational times were compared at each step. The process continued until further reductions in grid size resulted in negligible differences in the results, indicating an optimal point where increased computational effort did not yield significant benefits. A sensitivity analysis was performed to determine the optimal size and structure, examining various grid configurations and dimensions. Starting with a total grid element count of 1,294,362 and reaching up to 10,092,000, a total of 11 different models were compared in terms of hydrodynamics, morphodynamics, and computational time. Based on these studies, a grid configuration was selected where the grid size was uniform throughout the domain but refined near the seabed to 0.0375 m. This resulted in a grid size of 0.0375 m near the seabed and up to 0.15 m near the water surface, totaling 3,597,798 grid elements in the computational domain. The grid configuration used in the numerical model studies is detailed in Figure 3.

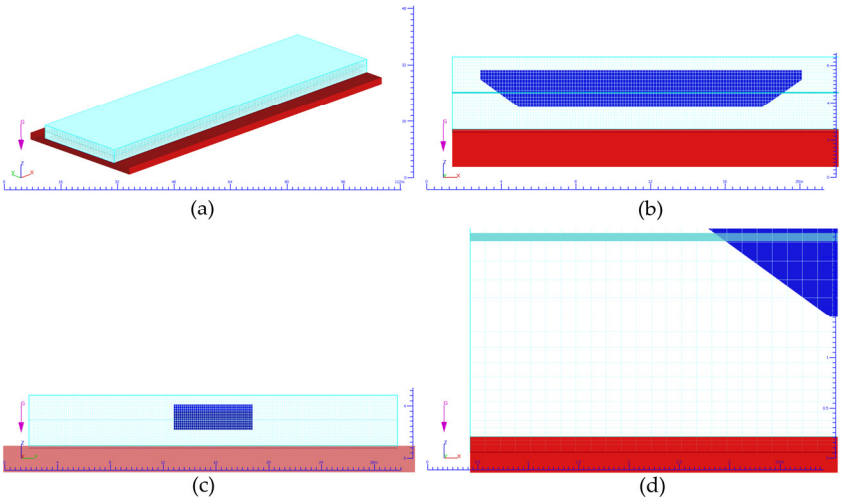

Figure 3. Grid structure used in the numerical model: (**a**) Isometric view, (**b**) side view, (**c**) front view, and (**d**) side view of the refined grid structure near the seabed.

The computational domain was configured with carefully selected boundary conditions to accurately represent the physical system under investigation. Given that the study focuses solely on the effects of the floating object and sediment interactions, with

no external forces other than atmospheric pressure considered, the following boundary conditions were implemented.

1. Minimum Z-axis Boundary: A "wall" boundary condition was imposed to represent the solid bottom of the domain.
2. Maximum Z-axis Boundary: An "atmospheric pressure" condition was applied to simulate the open air interface at the top of the domain.
3. Minimum and Maximum Y-axis Boundaries: "Symmetry" boundary conditions were employed on both sides to represent an infinitely wide domain and minimize edge effects.
4. Minimum and Maximum X-axis Boundaries: "Outflow" boundary conditions were set at both the inlet and outlet to allow for unrestricted flow through the domain.

The boundary conditions defined at each boundary, along with the floating object and seabed, are shown in Figure 4. In Figure 4, the area shown in red represents the seabed, and the blue object represents the floating object.

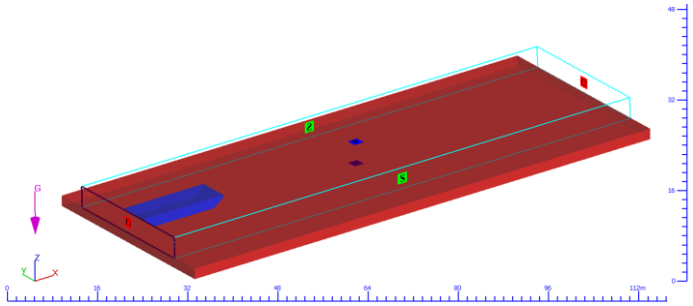

Figure 4. Computational domain, boundary conditions defined at the domain boundaries, and the floating object. Boundary condition labels: *S*-symmetry, *O*-outflow, *P*-atmospheric pressure, *W*-wall.

The floating object in this study was modeled using the General Moving Object (GMO) feature in the FLOW-3D software. This advanced computational fluid dynamics (CFD) tool offers versatile options for simulating object motion within fluid environments. The GMO feature allows for either pre-defined motion paths or dynamic, flow-coupled movement of the object. The motion can be specified with six degrees of freedom or constrained to specific axes or points, providing flexibility in modeling various real-world scenarios.

In the context of coupled-motion modeling, the software enables the specification of forces or torques acting on the floating object, allowing for a more realistic simulation of object–fluid interactions. This capability is particularly valuable in studies involving complex hydrodynamic effects.

For the purposes of this investigation, a controlled movement approach was adopted. The floating object was configured to be towed along the X-axis consistently across all scenarios. To maintain the desired motion characteristics, translation along the Y-axis was restricted to prevent lateral drift; rotation around the Z-axis was constrained to avoid yawing motion and movements; and rotations in other directions were left unconstrained to allow for natural responses to hydrodynamic forces.

This configuration ensured that the object's movement accurately represented the towing conditions being studied while still allowing for realistic interactions with the surrounding fluid environment.

The median grain diameter of the sediment considered in the studies was 0.0625 mm, with a specific gravity of 2650 kg/m^3, a bed-load transport coefficient of 0.06, and a drag coefficient of 0.018. The critical Shields parameter was calculated at each time step using the Soulsby–Whitehouse (1997) formula. For sediment transport calculations, the Van Rijn Transport Equation was employed. This well-established formula is particularly suitable

for predicting sediment movement in coastal and river environments. The comprehensive list of parameters used in the numerical modeling studies is presented in Table 1.

Table 1. Model parameters used in the numerical modeling studies.

Number of Sediment Species	Sediment Diameter (mm)	Sediment Density (kg/m^3)	Critical Shields Number	Entrainment Coefficient	Bed-Load Coefficient	Angle of Repose (°)	Bed-Load Transport Equation	Bed Roughness/d_{50} Ratio	External Force (Such as Wind, Wave, Current, etc.)
1	0.0625	2650	Every time step from Soulsby–Whitehouse equation	0.018	0.06	40	Van Rijn [20]	2.50	No

In the numerical model, the density of the floating object was adjusted to achieve the desired clearance height between the object's bottom and the seabed. Accelerations were kept constant across all scenarios to eliminate differences in model results due to acceleration. The duration of each simulation was determined based on the towing speed of the floating object and the 100 m length of the computational domain. This approach ensures that each simulation captures the full trajectory of the object through the domain while maintaining computational efficiency.

The numerical model scenarios, encompassing a total of 96 distinct simulations, are comprehensively presented in Table 2. These tables provide a detailed overview of each scenario, including specific parameters such as floating object type, dimensions, towing speed, and clearance height, allowing for systematic comparison and analysis across the range of simulated conditions.

Table 2. Numerical model scenarios.

Bow Type	Length (m)	Width (m)	Towing Speed (m/s)	Clearance Height (m)	Corresponding Scenarios
Blunt	15	6.0	2.0	0.4, 0.8, 1.0, 1.2	1, 2, 3, 4
			1.5	0.4, 0.8, 1.0, 1.2	5, 6, 7, 8
			1.0	0.4, 0.8, 1.0, 1.2	9, 10, 11, 12
			0.5	0.4, 0.8, 1.0, 1.2	13, 14, 15, 16
	15	6.9	2.0	0.4, 0.8, 1.0, 1.2	17, 18, 19, 20
			1.5	0.4, 0.8, 1.0, 1.2	21, 22, 23, 24
			1.0	0.4, 0.8, 1.0, 1.2	25, 26, 27, 28
			0.5	0.4, 0.8, 1.0, 1.2	29, 30, 31, 32
	17.25	6.0	2.0	0.4, 0.8, 1.0, 1.2	33, 34, 35, 36
			1.5	0.4, 0.8, 1.0, 1.2	37, 38, 39, 40
			1.0	0.4, 0.8, 1.0, 1.2	41, 42, 43, 44
			0.5	0.4, 0.8, 1.0, 1.2	45, 46, 47, 48
Raked	15	6.0	2.0	0.4, 0.8, 1.0, 1.2	49, 50, 51, 52
			1.5	0.4, 0.8, 1.0, 1.2	53, 54, 55, 56
			1.0	0.4, 0.8, 1.0, 1.2	57, 58, 59, 60
			0.5	0.4, 0.8, 1.0, 1.2	61, 62, 63, 64
	15	6.9	2.0	0.4, 0.8, 1.0, 1.2	65, 66, 67, 68
			1.5	0.4, 0.8, 1.0, 1.2	69, 70, 71, 72
			1.0	0.4, 0.8, 1.0, 1.2	73, 74, 75, 76
			0.5	0.4, 0.8, 1.0, 1.2	77, 78, 79, 80
	17.25	6.0	2.0	0.4, 0.8, 1.0, 1.2	81, 82, 83, 84
			1.5	0.4, 0.8, 1.0, 1.2	85, 86, 87, 88
			1.0	0.4, 0.8, 1.0, 1.2	89, 90, 91, 92
			0.5	0.4, 0.8, 1.0, 1.2	93, 94, 95, 96

4. Results

A comprehensive set of numerical model studies was conducted to investigate the complex interactions between floating object characteristics, hydrodynamic effects, and sediment dynamics. The simulations systematically varied key parameters including floating object geometry (comparing blunt and raked bow designs), towing speed, clearance height (the distance between the object and the seabed), and sediment properties. These parameters were carefully selected to encompass a wide range of realistic scenarios, as detailed in Table 2.

The primary objectives of these simulations were to quantify the hydrodynamic effects induced by the floating object and determine the resulting suspended sediment concentration under various conditions. This approach allowed for a thorough examination of how different object designs and operational parameters influence sediment transport in marine environments.

Figures 5–12 illustrate the flow characteristics around the floating objects through velocity fields and flow directions. Specifically, Figures 5–8 demonstrate these patterns for blunt bow configurations, showing velocity distributions and flow development in multiple views (plan, near-bed, and longitudinal sections). The corresponding results for raked bow configurations (Figures 9–12) enable direct comparison of how bow geometry influences these flow patterns.

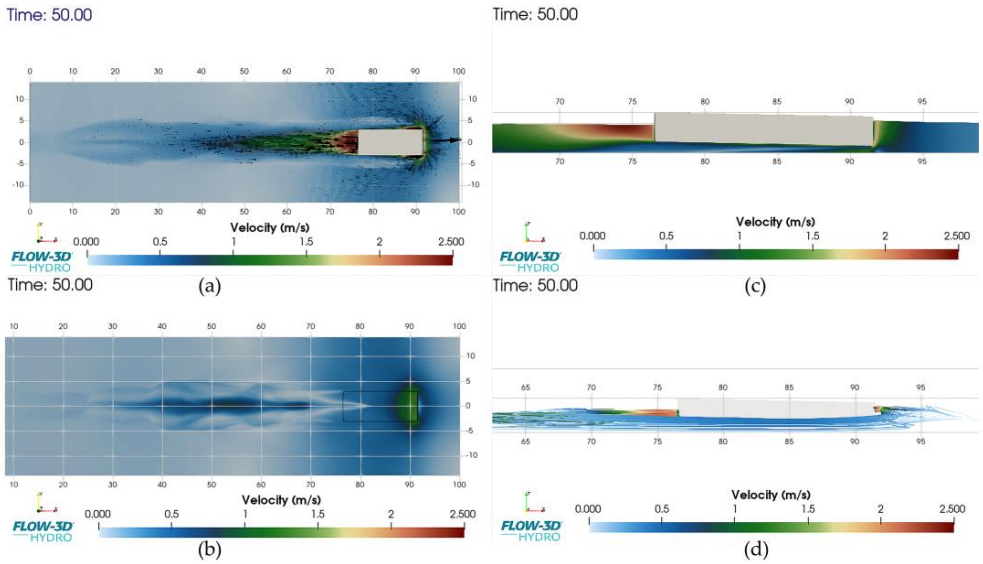

Figure 5. Flow velocities and directions at the end of the simulation for Scenario 2, presented in four views: (**a**) Plan view of flow velocities in the computational domain, (**b**) plan view of flow velocities on the seabed, (**c**) longitudinal sectional view of flow velocities along the X-axis at the mid-point of the Y-axis, (**d**) longitudinal sectional view of flow streamlines along the X-axis at the mid-point of the Y-axis.

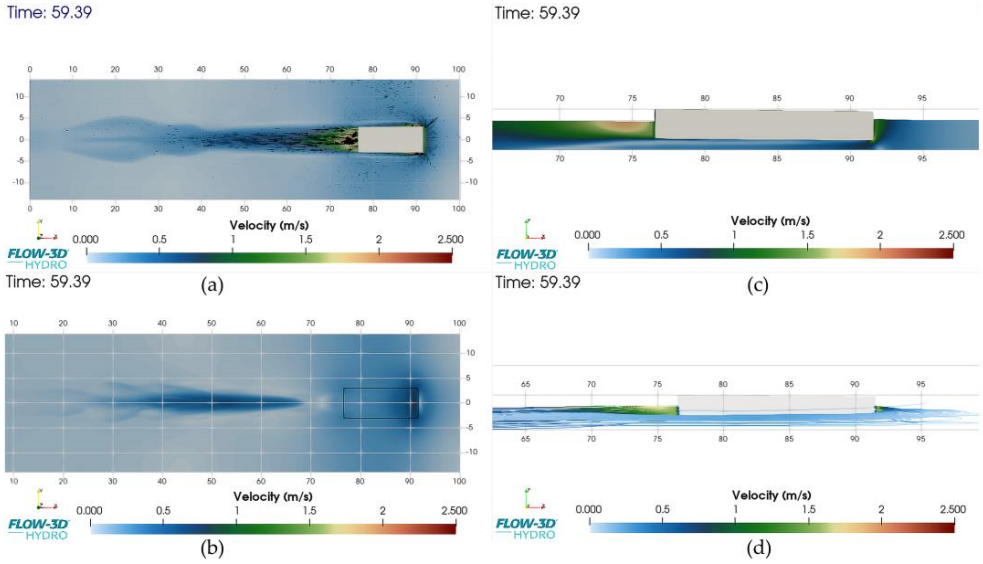

Figure 6. Flow velocities and directions at the end of the simulation for Scenario 6, presented in four views: (**a**) Plan view of flow velocities in the computational domain, (**b**) plan view of flow velocities on the seabed, (**c**) longitudinal sectional view of flow velocities along the X-axis at the mid-point of the Y-axis, (**d**) longitudinal sectional view of flow streamlines along the X-axis at the mid-point of the Y-axis.

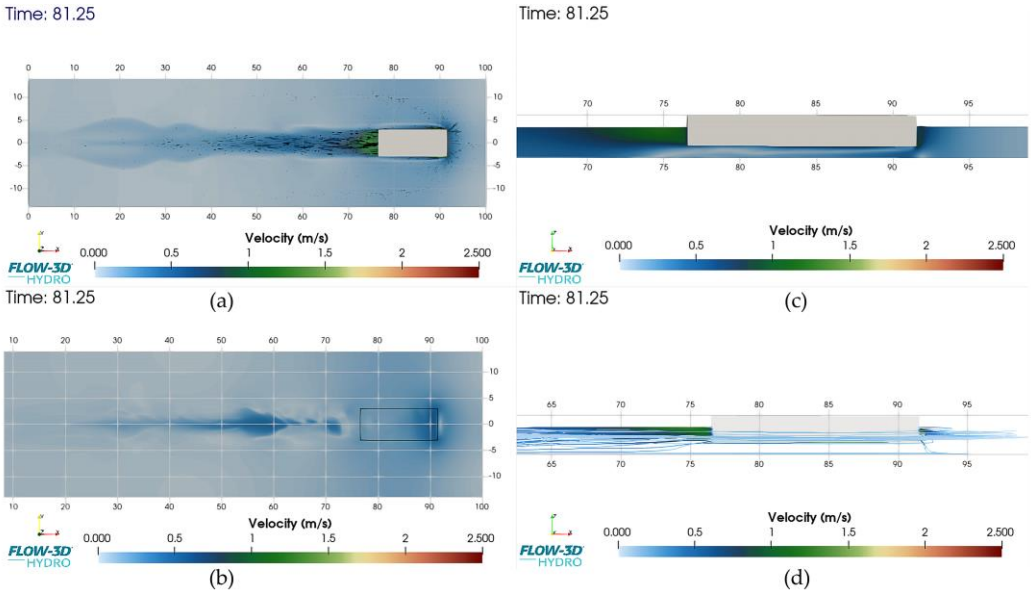

Figure 7. Flow velocities and directions at the end of the simulation for Scenario 10, presented in four views: (**a**) Plan view of flow velocities in the computational domain, (**b**) plan view of flow velocities on the seabed, (**c**) longitudinal sectional view of flow velocities along the X-axis at the mid-point of the Y-axis, (**d**) longitudinal sectional view of flow streamlines along the X-axis at the mid-point of the Y-axis.

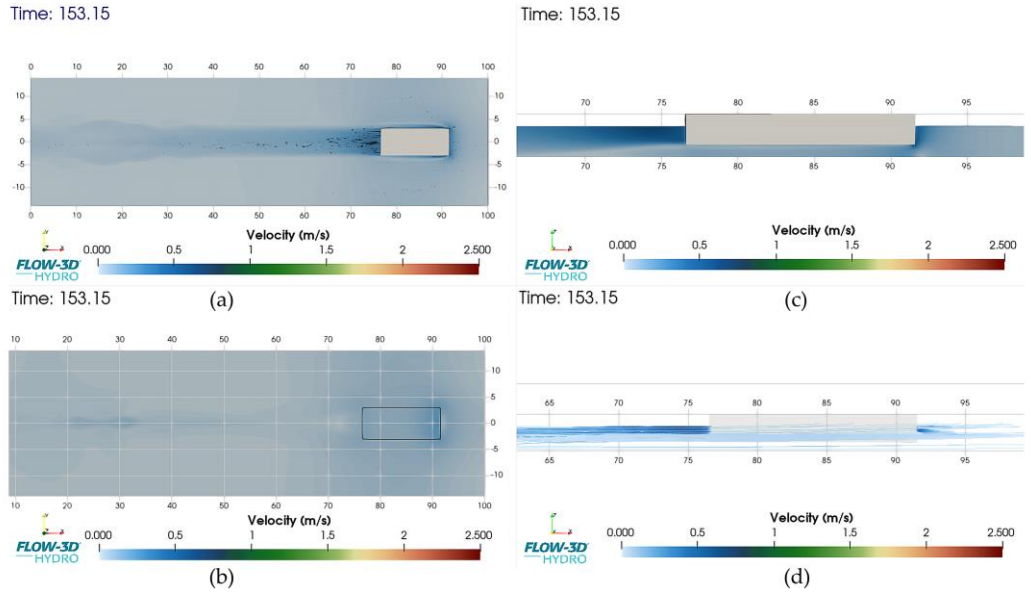

Figure 8. Flow velocities and directions at the end of the simulation for Scenario 14, presented in four views: (**a**) Plan view of flow velocities in the computational domain, (**b**) plan view of flow velocities on the seabed, (**c**) longitudinal sectional view of flow velocities along the X-axis at the mid-point of the Y-axis, (**d**) longitudinal sectional view of flow streamlines along the X-axis at the mid-point of the Y-axis.

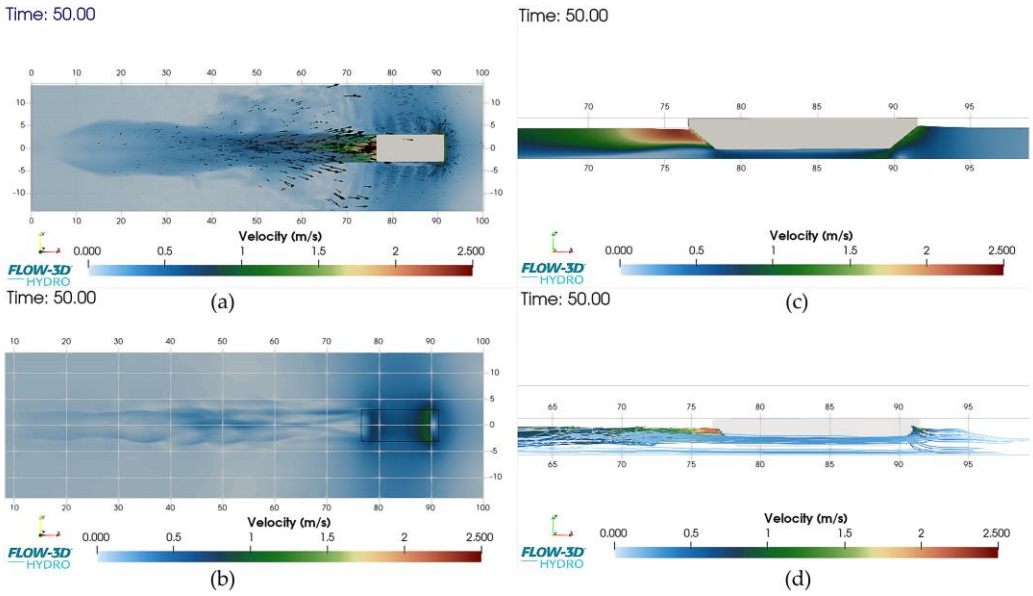

Figure 9. Flow velocities and directions at the end of the simulation for Scenario 50, presented in four views: (**a**) Plan view of flow velocities in the computational domain, (**b**) plan view of flow velocities on the seabed, (**c**) longitudinal sectional view of flow velocities along the X-axis at the mid-point of the Y-axis, (**d**) longitudinal sectional view of flow streamlines along the X-axis at the mid-point of the Y-axis.

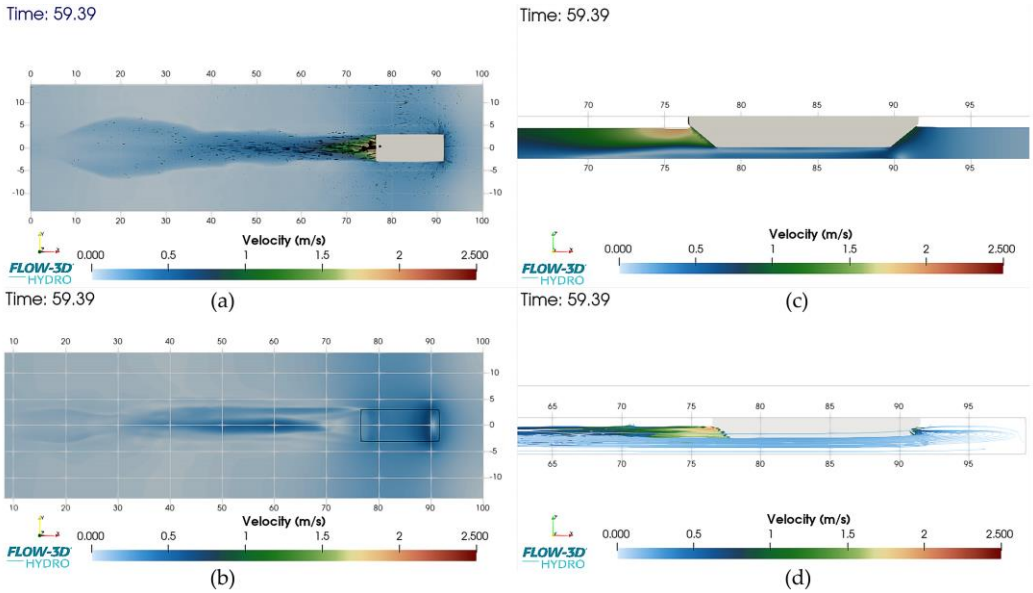

Figure 10. Flow velocities and directions at the end of the simulation for Scenario 54, presented in four views: (**a**) Plan view of flow velocities in the computational domain, (**b**) plan view of flow velocities on the seabed, (**c**) longitudinal sectional view of flow velocities along the X-axis at the mid-point of the Y-axis, (**d**) longitudinal sectional view of flow streamlines along the X-axis at the mid-point of the Y-axis.

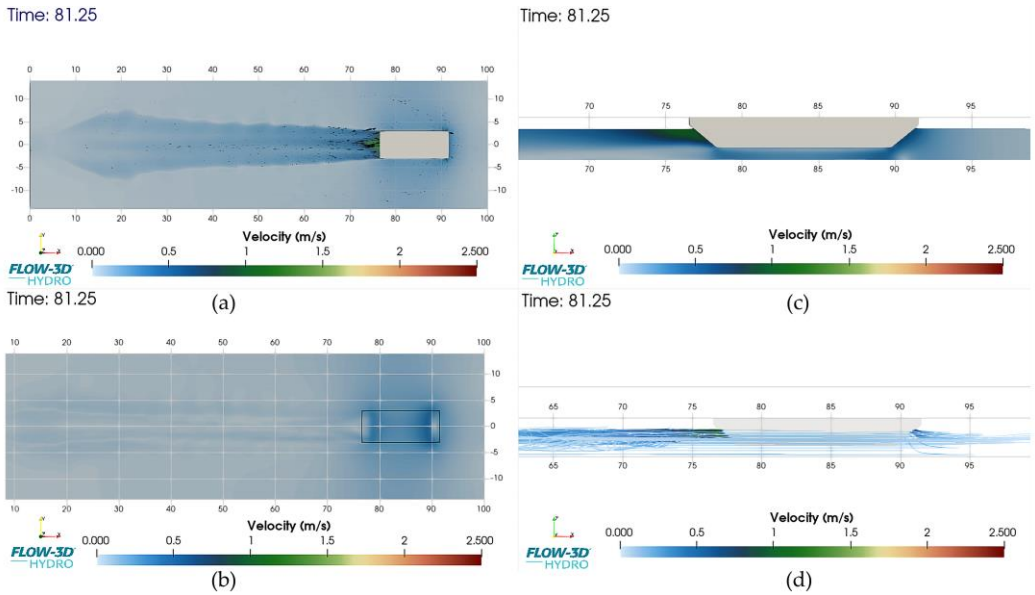

Figure 11. Flow velocities and directions at the end of the simulation for Scenario 58, presented in four views: (**a**) Plan view of flow velocities in the computational domain, (**b**) plan view of flow velocities on the seabed, (**c**) longitudinal sectional view of flow velocities along the X-axis at the mid-point of the Y-axis, (**d**) longitudinal sectional view of flow streamlines along the X-axis at the mid-point of the Y-axis.

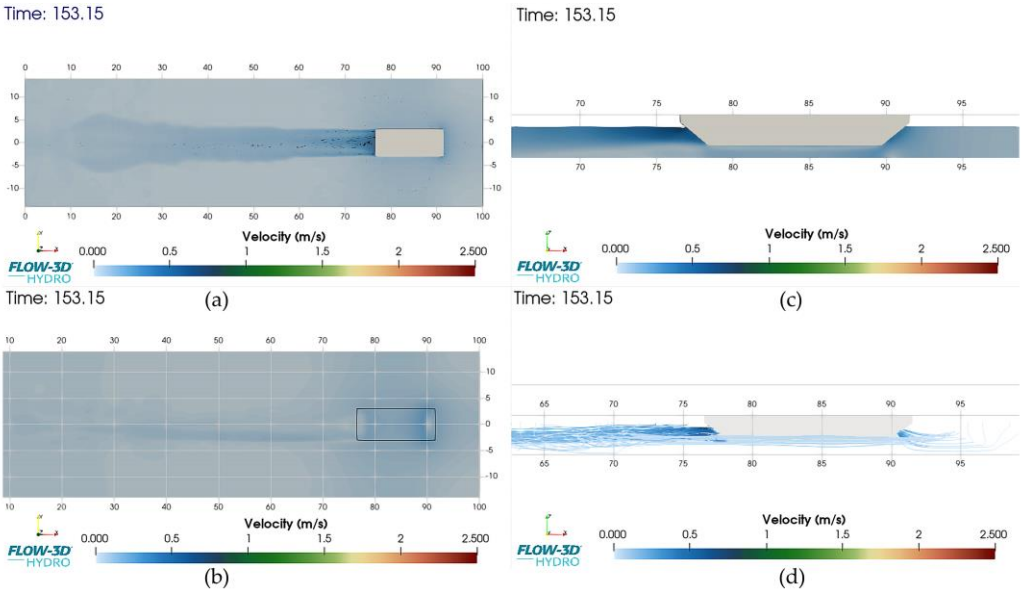

Figure 12. Flow velocities and directions at the end of the simulation for Scenario 62, presented in four views: (**a**) Plan view of flow velocities in the computational domain, (**b**) plan view of flow velocities on the seabed, (**c**) longitudinal sectional view of flow velocities along the X-axis at the mid-point of the Y-axis, (**d**) longitudinal sectional view of flow streamlines along the X-axis at the mid-point of the Y-axis.

Figures 13–20 present the resulting morphological effects, including seabed shear velocities, suspended sediment concentrations, and bed level changes for both configurations. These visualizations demonstrate how the different flow patterns translate into sediment mobilization and transport mechanisms.

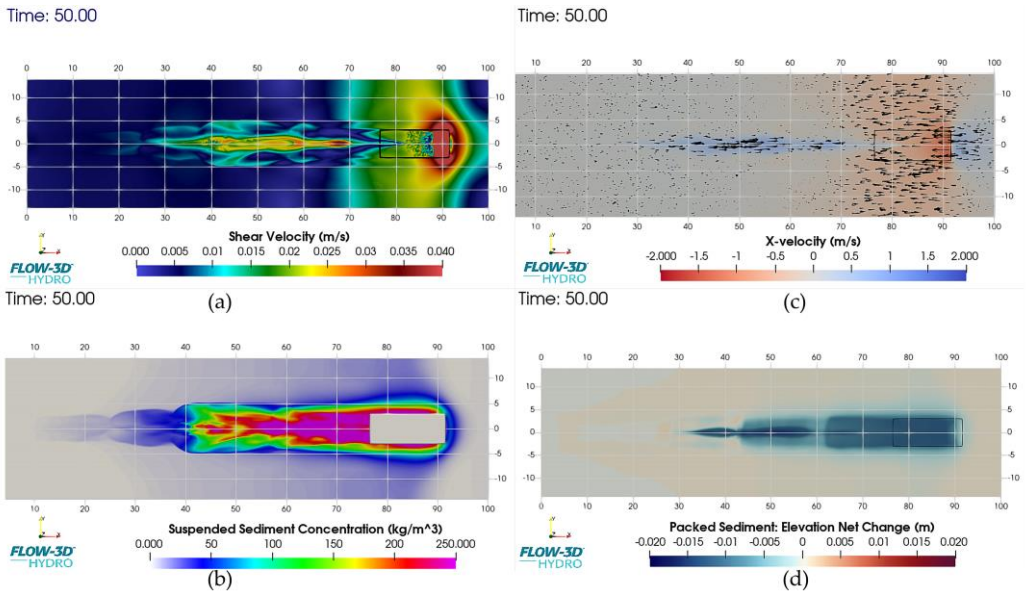

Figure 13. Hydromorphological effects occurring in the computational domain at the end of the simulation for Scenario 2, displayed as follows: (**a**) Plan view of shear velocities on the seabed, (**b**) plan view of suspended sediment concentrations, (**c**) plan view of flow velocities along the X-axis on the seabed, (**d**) plan view of morphological changes on the seabed.

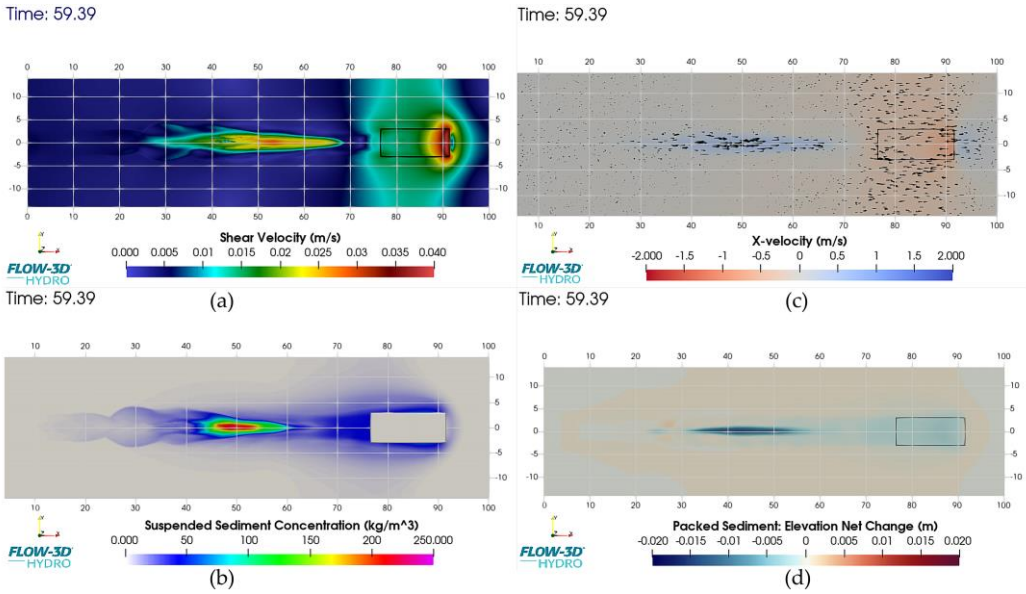

Figure 14. Hydromorphological effects occurring in the computational domain at the end of the simulation for Scenario 6, displayed as follows: (**a**) Plan view of shear velocities on the seabed, (**b**) plan view of suspended sediment concentrations, (**c**) plan view of flow velocities along the X-axis on the seabed, (**d**) plan view of morphological changes on the seabed.

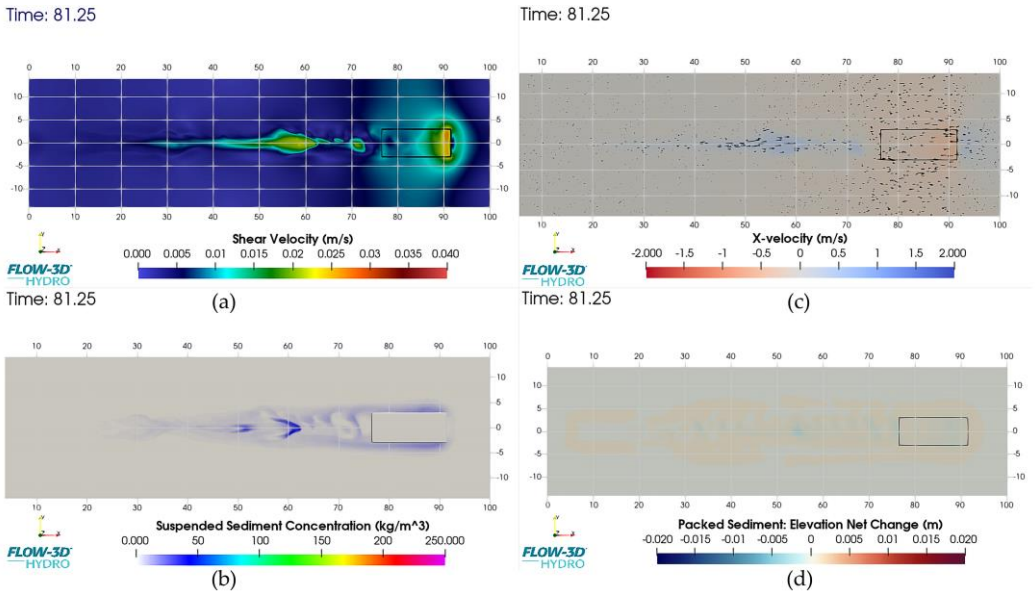

Figure 15. Hydromorphological effects occurring in the computational domain at the end of the simulation for Scenario 10, displayed as follows: (**a**) Plan view of shear velocities on the seabed, (**b**) plan view of suspended sediment concentrations, (**c**) plan view of flow velocities along the X-axis on the seabed, (**d**) plan view of morphological changes on the seabed.

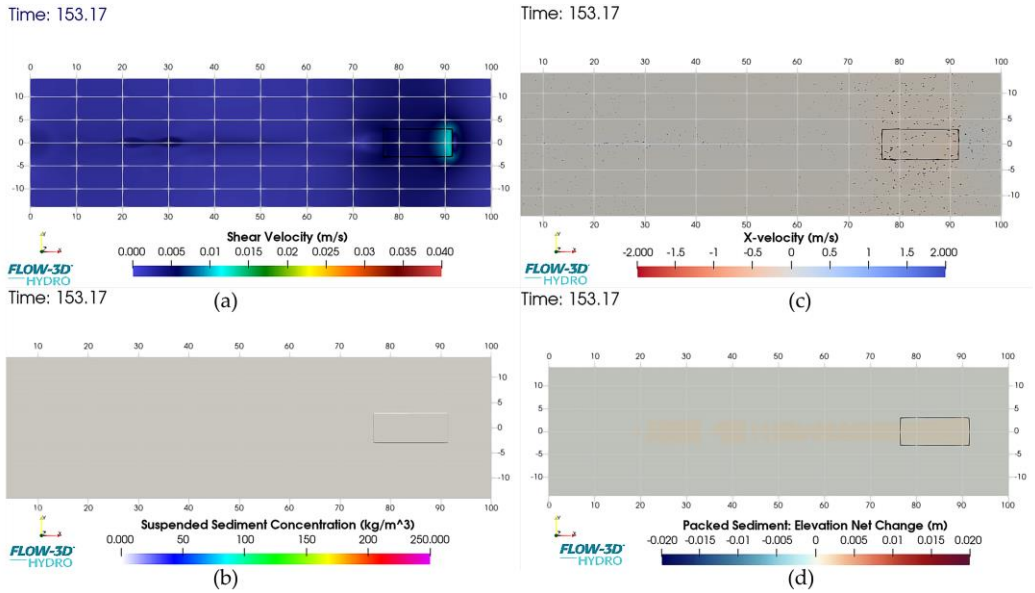

Figure 16. Hydromorphological effects occurring in the computational domain at the end of the simulation for Scenario 14, displayed as follows: (**a**) Plan view of shear velocities on the seabed, (**b**) plan view of suspended sediment concentrations, (**c**) plan view of flow velocities along the X-axis on the seabed, (**d**) plan view of morphological changes on the seabed.

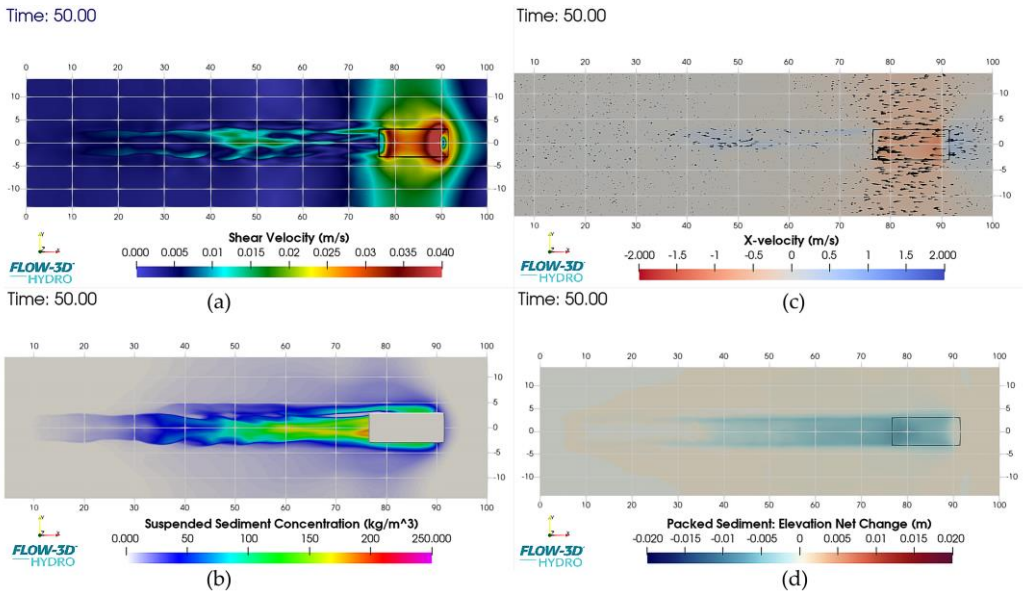

Figure 17. Hydromorphological effects occurring in the computational domain at the end of the simulation for Scenario 50, displayed as follows: (**a**) plan view of shear velocities on the seabed, (**b**) plan view of suspended sediment concentrations, (**c**) plan view of flow velocities along the X-axis on the seabed, (**d**) plan view of morphological changes on the seabed.

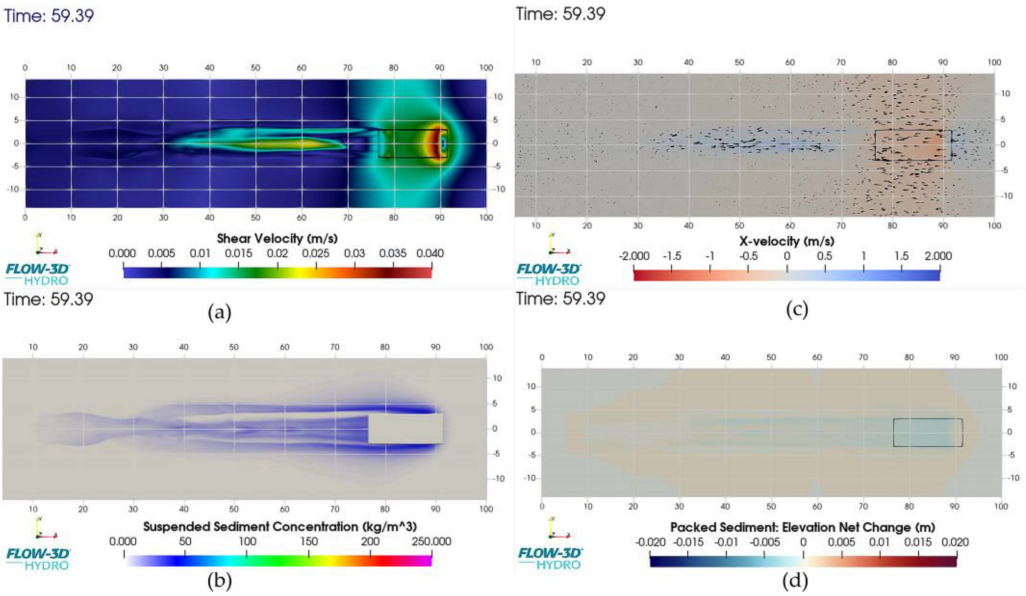

Figure 18. Hydromorphological effects occurring in the computational domain at the end of the simulation for Scenario 54, displayed as follows: (**a**) Plan view of shear velocities on the seabed, (**b**) plan view of suspended sediment concentrations, (**c**) plan view of flow velocities along the X-axis on the seabed, (**d**) plan view of morphological changes on the seabed.

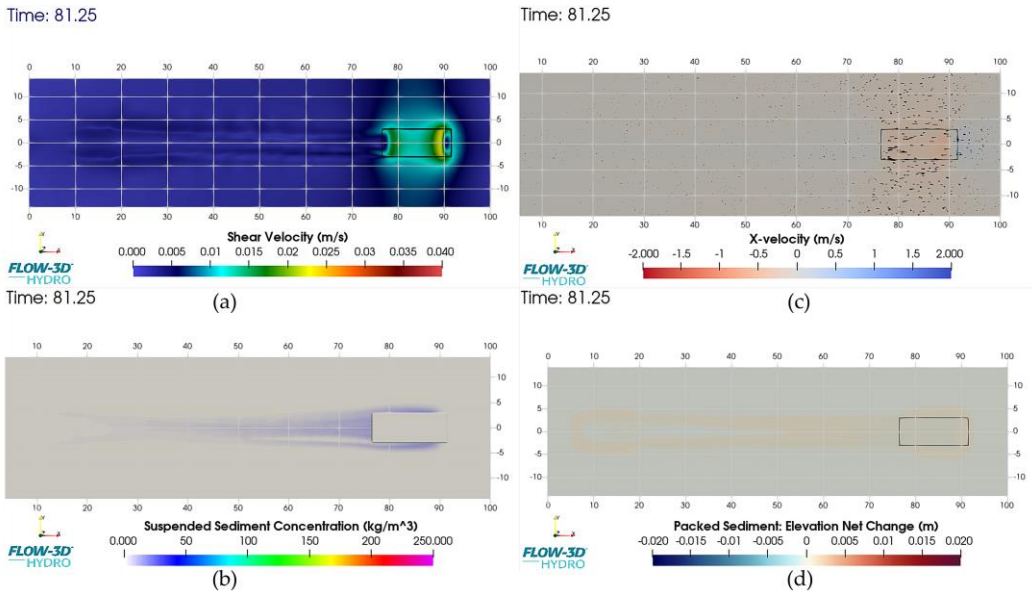

Figure 19. Hydromorphological effects occurring in the computational domain at the end of the simulation for Scenario 58, displayed as follows: (**a**) Plan view of shear velocities on the seabed, (**b**) plan view of suspended sediment concentrations, (**c**) plan view of flow velocities along the X-axis on the seabed, (**d**) plan view of morphological changes on the seabed.

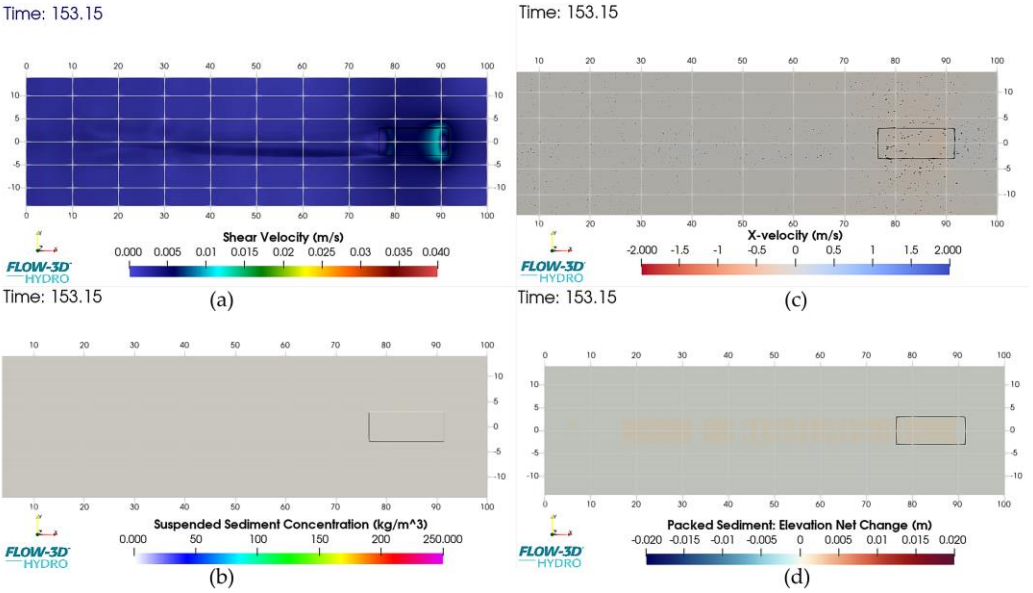

Figure 20. Hydromorphological effects occurring in the computational domain at the end of the simulation for Scenario 62, displayed as follows: (**a**) Plan view of shear velocities on the seabed, (**b**) plan view of suspended sediment concentrations, (**c**) plan view of flow velocities along the X-axis on the seabed, (**d**) plan view of morphological changes on the seabed.

Figures 21–23 provide comparative analyses of the relationships between operational parameters and sediment resuspension, quantifying how towing speed, clearance height, and geometric parameters influence suspended sediment concentrations.

The numerical simulations revealed complex flow patterns around the floating objects, with significant variations observed based on object geometry, towing speed, and clearance height. Figures 5–8 illustrate the flow velocities and directions resulting from towing a floating object with a blunt bow at various speeds, maintaining a constant clearance height of 0.80 m. A notable observation was the pronounced squat effect at higher towing speeds,

particularly at 2 m/s, where the floating object exhibited a greater proximity to the seabed. This effect demonstrated a direct relationship with towing speed, intensifying as speeds increased and diminishing as speeds decreased. The squat effect significantly influenced the flow dynamics beneath the floating object. Peak flow velocities were consistently observed beneath the bow section, with a gradual decrease in magnitude progressing towards the stern. This velocity gradient is attributed to the pressure differential created by the object's movement through the water.

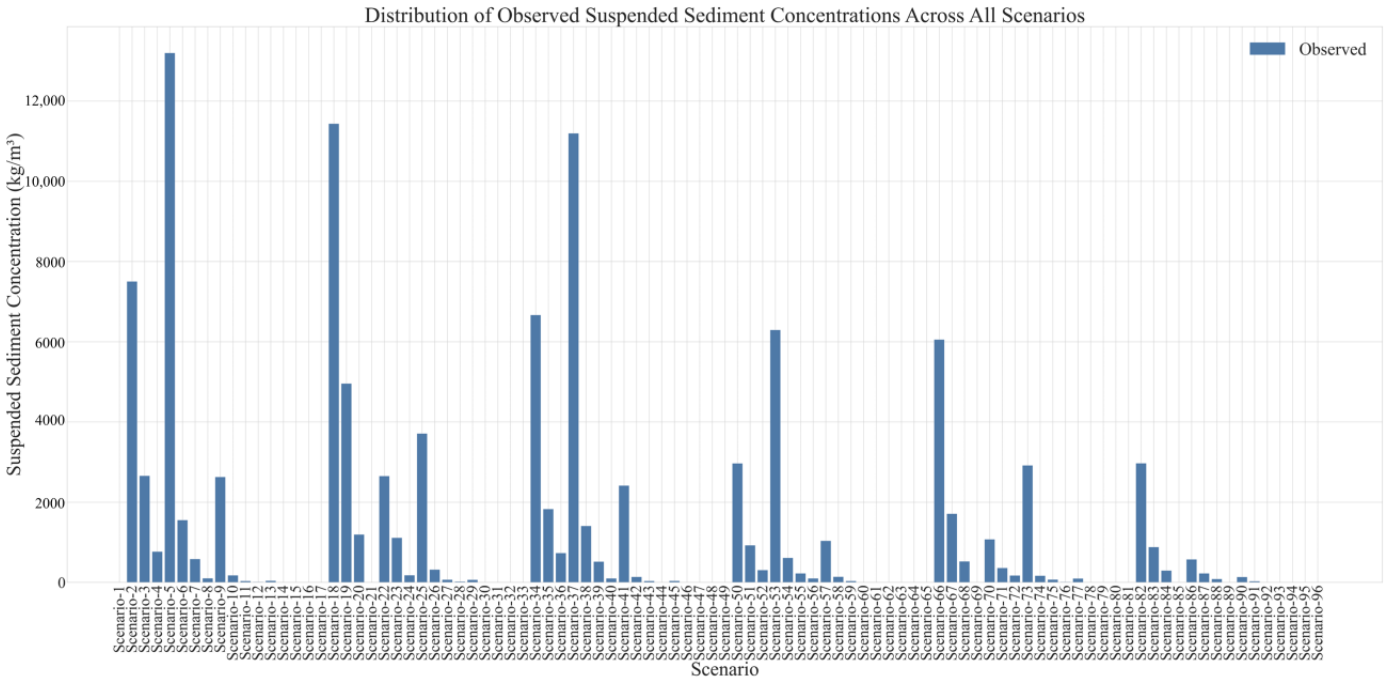

Figure 21. Distribution of suspended sediment concentrations across all scenarios.

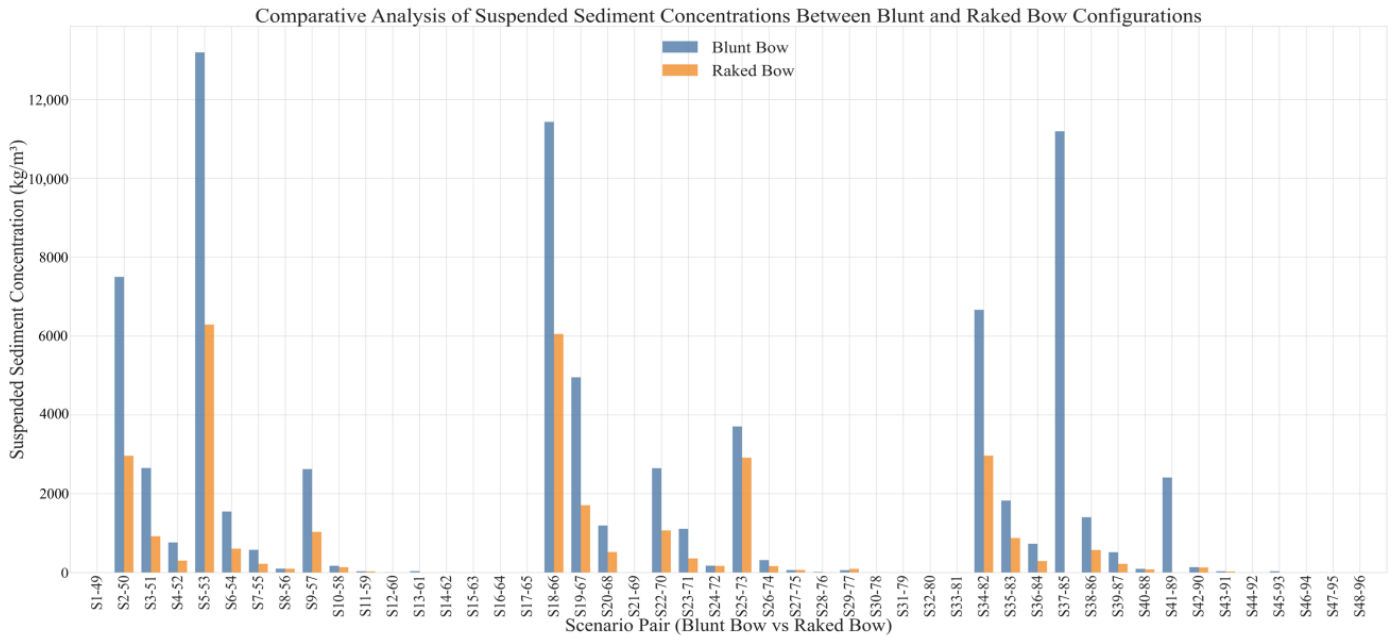

Figure 22. Comparative analysis of suspended sediment concentrations between blunt and raked bow configurations.

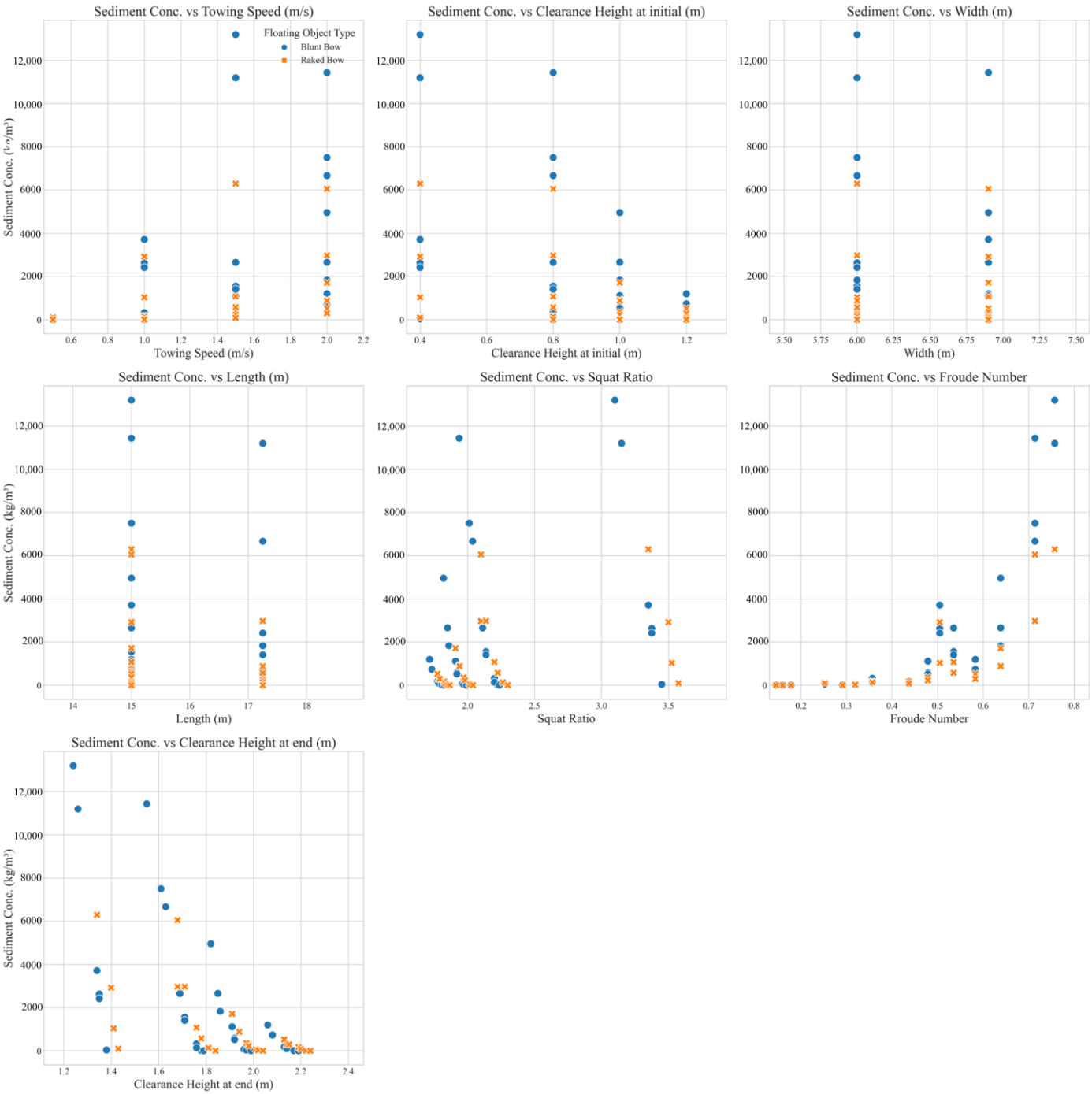

Figure 23. Sediment concentration according to various geometrical and hydrodynamic parameters for blunt and raked bow floating objects.

Analysis of the model outputs for the blunt bow (Figures 5–8) revealed distinct hydrodynamic characteristics compared to the raked bow (Figures 9–12) configuration. The blunt bow geometry resulted in a more substantial displacement of water at the front of the object. This led to elevated water levels in the bow region, creating a pronounced pressure gradient between the high-pressure area at the bow and the low-pressure zone beneath the floating object. Consequently, this pressure differential induced higher flow velocities under the object. However, it is important to note that in certain operational conditions, the raked bow can also exhibit significant flow velocities and sediment resuspension depending on towing speed and clearance height.

An increase in the object's width, irrespective of bow shape, resulted in a greater volume of displaced water at the front. This amplified the instantaneous potential energy in this region compared to the baseline case. The heightened energy state translated into increased flow velocities beneath the floating object. Interestingly, increasing the object's length did not produce significant visual alterations in the flow patterns compared to the standard configuration. However, quantitative analysis of the numerical results indicated a slight reduction in flow velocities. This subtle effect warrants further investigation to fully understand the hydrodynamic implications of object elongation.

The limited influence of object length on flow patterns can be attributed to the dominance of bow geometry, towing speed, and clearance height in shaping the hydrodynamic field. While length may play a role in certain scenarios, its effect is overshadowed by these more critical parameters, particularly in shallow water conditions where flow confinement and proximity to the seabed are pronounced.

Following the analysis of flow dynamics, attention is now directed towards the morphodynamic effects and sediment suspension patterns observed in the numerical simulations. This comprehensive examination provides crucial insights into the complex interactions between floating objects and the seabed environment.

At the conclusion of each scenario, the morphodynamic effects in the computational domain, flow velocities along the X-axis on the seabed, and shear velocities occurring on the seabed are presented in Figures 13–20. These figures provide a comprehensive visualization of the seabed interactions induced by the floating object under various conditions. Figures 13–16 illustrate the results for the floating object with a blunt bow, while Figures 17–20 depict the outcomes for the raked bow design. This comparative presentation enables a direct assessment of how bow geometry influences seabed interactions across different scenarios.

The model results presented in Figures 13–20 reveal a significant correlation between towing speed and seabed shear velocities. These hydrodynamic patterns directly influence sediment resuspension characteristics. Quantitative analysis of suspended sediment concentrations demonstrates that blunt bow configurations consistently generate higher values compared to raked geometries under identical operational conditions. Specifically, for cases with significant sediment mobilization (concentrations exceeding 1000 kg/m^3), blunt bows increase suspended sediment concentrations by 90–190% relative to raked configurations. This enhancement exhibits strong correlation with the Froude number, as increased towing speeds amplify the differences between bow geometries through the combined effects of bow-induced pressure gradients and squat-related clearance reduction.

At the maximum towing speed of 2 m/s, substantially elevated shear velocities were observed on the seabed compared to lower-speed scenarios. Peak shear velocities were consistently recorded in the vicinity of the floating object's bow, particularly in the area directly beneath it. This localized increase in shear stress resulted in predominant scouring beneath the bow region and correspondingly elevated suspended sediment concentrations.

To compare the total amounts of suspended sediment generated across all scenarios, Figures 21–23 were prepared to provide key insights into the various parameters of suspended sediment based on different geometrical and operational configurations. Figures 22 and 23 further provide a comparative evaluation between blunt and raked bow configurations, demonstrating the significant role of bow geometry in determining sediment resuspension dynamics.

The results of the simulations at varying towing speeds indicate that the highest towing speed of 2 m/s produces the most intense hydrodynamic effects on the seabed. Specifically, the highest shear velocities were noted beneath and around the bow of the floating object. Consequently, scouring occurred predominantly beneath the bow, and the amount of suspended sediment reached higher values particularly in this region. The observed shear velocities at this towing speed were substantially higher than those in

lower-speed scenarios, supporting the conclusion that increased towing speeds are directly correlated with higher sediment disturbance.

As the width of the floating object increased, a noticeable increase in flow velocities throughout the domain was observed. At the highest towing speed, the flow velocities beneath the floating object increased by approximately 50%, with this effect diminishing at lower speeds. This widening led to greater water displacement at the front, regardless of bow shape, resulting in higher water levels and increased return flow velocities. The significant water movement from the high-pressure zone near the bow to the low-pressure area beneath the object explains the increased shear and flow velocities, leading to intensified scouring and sediment resuspension over a larger area.

In contrast, changes in the length of the floating object had a less substantial impact on the flow dynamics. While there were some minor variations in flow velocity and direction, the overall effect of length was less pronounced compared to width, with the primary observable change being a gradual decrease in velocity from bow to stern.

The comparison between blunt and raked bow configurations revealed that, while the general flow patterns remained consistent, the raked bow generally exhibited lower overall flow velocities due to its streamlined shape, which reduced sediment resuspension and scouring. However, under high towing speeds or reduced clearance heights, even raked bows can induce notable hydrodynamic effects, although typically less pronounced than those observed with blunt bows. These results indicate that blunt bow geometries have a more significant impact on sediment transport compared to raked bows, especially under similar operational conditions.

Finally, among all the evaluated parameters, towing speed was confirmed as the most influential factor in determining hydrodynamic and morphological changes. Higher towing speeds increase the squat effect, bringing the floating object closer to the seabed, which leads to an increase in flow velocities and sediment movement. Conversely, reduced towing speeds result in diminished hydrodynamic effects. Clearance height was identified as the next most critical parameter, with lower clearance heights intensifying the interaction between the floating object and the seabed, and higher clearance heights alleviating these effects.

4.1. Regression Analysis

To quantitatively assess the influence of various parameters on sediment resuspension, a multivariate polynomial regression analysis was conducted using the results from the numerical simulations. The objective was to develop a predictive model that accurately estimates the suspended sediment amount based on key variables such as towing speed, time, squat ratio, and floating object type.

4.1.1. Data Preparation and Transformation

The dataset comprised results from 84 simulation scenarios, encompassing variations in towing speed, squat ratio, time, and floating object bow types. To meet the assumptions of linear regression regarding normality and homoscedasticity, a Box–Cox transformation was applied to the dependent variable—the suspended sediment concentration (S, in kg/m^3). This transformation serves to stabilize variance and approximate normal distribution, thereby enhancing the reliability and validity of the regression model.

Additionally, the independent variables were scrutinized for multicollinearity using Variance Inflation Factor (VIF) analysis. Variables exhibiting high VIF values, indicative of strong multicollinearity, were iteratively removed to optimize model stability and interpretability. The final set of predictors included the Froude number (Fr), squat ratio (Sq), squared time (t^2), and floating object type (Obj_T), along with relevant interaction terms such as $Fr \times Obj\_T$, $Sq \times Obj\_T$, and $t^2 \times Obj\_T$.

4.1.2. Development of the Regression Model

A second-degree polynomial regression model was selected to capture potential nonlinear relationships among the variables. The independent variables incorporated in the model were as follows:

- Froude Number (*Fr*): A dimensionless parameter defined as $Fr = \frac{v}{\sqrt{g \times h}}$, where v is the towing speed and h is the clean clearance height.
- Squat Ratio (*Sq*): Represents the ratio of initial clearance height to final distance to the seabed ($Sq = \frac{c}{f}$).
- Time (*t*): Duration of towing (s), squared to capture nonlinear effects.
- Floating Object Type (*Obj_T*): Categorical variable representing bow shape (0 for blunt bow, 1 for raked bow).
- Interaction Terms:
  - $Fr \times Obj\_T$: Interaction between Froude_Number and *Obj_T*,
  - $Sq \times Obj\_T$: Interaction between squat ratio and *Obj_T*,
  - $t^2 \times$ Obj_T: Interaction between squared time and Obj_T.

The regression equation for the Box–Cox-transformed suspended sediment concentration is expressed as follows:

$$BoxCox(S) = 7.80 + 5.11 \times Fr + 1.1 \times Sq - 0.79 \times t^2 - 1.06 \times Obj_T - 0.72 \times \mathrm{Fr} \times Obj_T + 0.12 \times Sq \times Obj_T - 0.08 \times \mathrm{Obj\_T} \quad (15)$$

where

S = suspended sediment concentration (kg/m^3),
t = time (s),
Sq = squat ratio,
Obj_T = floating object type (0 for blunt bow, 1 for raked bow),
Fr = Froude number.

The summary statistics of the regression model, including coefficients, standard errors, *t*-values, and *p*-values, are presented in Table 3 for each term.

Table 3. Summary of regression coefficients and statistical significance.

Term	Coefficient	Std. Error	t-Value	*p*-Value
const	**7.7971**	**0.2673**	**29.1676**	**0.0**
Fr	**5.1125**	**0.2045**	**24.9989**	**0.0**
Sq	**1.095**	**0.1577**	**6.9429**	**0.0**
t_sq	**−0.7915**	**0.2045**	**−3.8712**	**0.0002**
Obj_T	**−1.0589**	**0.3822**	**−2.7706**	**0.007**
Fr_Obj_T	**−0.7154**	**0.2952**	**−2.4233**	**0.0178**
Sq_Obj_T	0.124	0.2504	0.4952	0.6219
t_sq_Obj_T	−0.0837	0.2961	−0.2826	0.7783

Note: Statistically significant terms at the 0.05 level are highlighted in bold.

4.1.3. Model Performance and Statistical Significance

The regression model demonstrated a robust explanatory power, with an R-squared value of 0.9647 and an adjusted R-squared of 0.9614. These metrics indicate that approximately 96.47% of the variability in the Box–Cox-transformed suspended sediment concentration is accounted for by the model. The F-statistic of 296.53 (Prob (F-statistic) = 1.83×10^{-52}) underscores the overall statistical significance of the regression model.

The analysis identified several statistically significant variables (*p*-value < 0.05), including the following:

- Froude number (Fr),
- Squat ratio (Sq),
- Squared time (t^2),
- Floating object type (Obj_T),
- Interaction between Fr and Obj_T ($Fr \times Obj\_T$).

These significant terms underscore the complex interplay between operational parameters and floating object characteristics in influencing sediment resuspension.

The residuals of the model were examined to assess the assumptions of normality. Figure 24 presents a normal Q-Q plot of these residuals, which, upon careful analysis, reveals a distribution closely approximating normality. This conformity to the expected pattern provides significant support for the fundamental assumptions of the regression model and increases confidence in its validity.

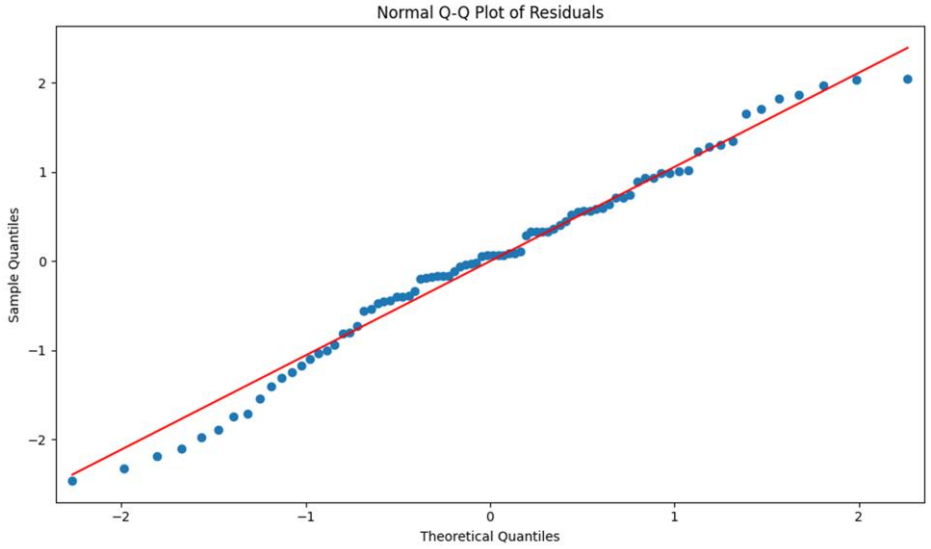

Figure 24. Normal Q-Q plot of model residuals.

4.1.4. Interpretation of Results

The regression analysis elucidates the significant roles of the Froude number (Fr), squat ratio (Sq), squared time (t^2), and floating object type (Obj_T) in predicting sediment resuspension, aligning with the findings from the numerical simulations. Specifically, higher Froude numbers substantially increase sediment resuspension due to enhanced flow velocities and shear stresses on the seabed.

Similarly, the squat ratio (Sq) exhibits a positive and significant relationship with sediment concentration, indicating that higher squat ratios amplify sediment resuspension. This is consistent with the observed increase in flow velocities beneath the floating object as the squat effect intensifies. Additionally, the floating object type (Obj_T) demonstrates a significant negative impact on sediment resuspension, suggesting that raked bow designs ($Obj\_T = 1$) are more effective in mitigating sediment disturbance compared to blunt bows ($Obj\_T = 0$). Also, the interaction term between the Froude number and object type ($Fr \times Obj\_T$) further refines this relationship, showing a negative coefficient of -0.7154 ($p = 0.018$). This interaction implies that the impact of the Froude number on sediment resuspension is moderated by the bow shape. This finding corroborates the hydrodynamic analyses, where blunt bows were observed to generate higher flow velocities beneath the object due to increased water displacement at the front.

4.1.5. Implications for Design and Operation

The regression model provides a valuable predictive tool for estimating sediment resuspension based on operational parameters and floating object characteristics. The strong positive relationship between the Froude number and sediment resuspension underscores the importance of optimizing towing speeds and clearance heights to mitigate environmental impacts. Lowering the Froude number by reducing towing speeds or increasing clearance heights can effectively decrease suspended sediment concentrations, thereby minimizing ecological disruptions in sensitive marine habitats.

The significant positive association of the squat ratio with sediment concentration emphasizes the need for careful consideration of floating object deformation under operational conditions. Designing floating structures with optimal squat ratios can reduce their propensity to disturb sediments. This can be achieved by selecting hull geometries that minimize deformation or by implementing structural features that stabilize the object's position relative to the seabed. Incorporating raked bow geometries can enhance the environmental performance of floating structures, making them more suitable for deployment in areas with sensitive benthic ecosystems.

Overall, the regression model serves as a valuable predictive tool that informs design choices and operational practices aimed at minimizing sediment resuspension. By leveraging the relationships identified in the model, engineers and operators can develop strategies that balance operational efficiency with environmental stewardship, fostering sustainable maritime activities.

4.1.6. Limitations and Future Work

While the regression model demonstrates strong predictive capabilities, it is important to acknowledge potential limitations. The dataset, comprising 84 simulation scenarios, while comprehensive, may not fully capture the diversity of real-world conditions encountered in marine environments. Expanding the dataset to include a broader range of operational scenarios and environmental conditions would enhance the model's generalizability and robustness. Additionally, the model's reliance on simulated data necessitates empirical validation through field studies to corroborate its predictive accuracy in natural settings.

While the findings provide valuable insights into the effects of towing speed, object geometry, and clearance height, it is important to note that environmental variables such as water depth, current fluctuations, and sediment composition were not incorporated into this study. Including these variables in future research would provide a more comprehensive understanding of the factors driving sediment resuspension and improve the model's predictive capabilities.

Future research should focus on addressing these limitations by expanding the dataset, incorporating additional environmental variables, and validating the model with empirical data. These efforts will contribute to the development of more accurate and reliable predictive models for sediment resuspension, thereby supporting sustainable design and operational practices in marine engineering.

5. Discussion

The findings of this study underscore the profound influence of hydrodynamic parameters and floating object geometry on sediment resuspension in marine environments. The regression analysis revealed that the Froude number and squat ratio are paramount in determining the extent of sediment disturbance caused by non-powered floating objects. The significant positive correlation between the Froude number and sediment concentration corroborates the existing literature that identifies vessel speed as a critical factor influencing sediment dynamics in shallow waters.

The squat ratio's positive association with sediment concentration highlights the role of object deformation in sediment dynamics. As the squat ratio increases, the floating object undergoes greater deformation, disrupting the water flow beneath and enhancing sediment suspension. This relationship emphasizes the necessity of optimizing floating object designs to minimize deformation under operational conditions, thereby reducing their environmental footprint.

While phenomena such as the squat effect and width–velocity relationships have been extensively studied for powered vessels, the results demonstrate distinct characteristics in non-powered cases. The absence of propeller-induced turbulence leads to pressure-dominated flow fields, resulting in different patterns of sediment mobilization. Specifically, the squat effect in non-powered objects shows stronger dependence on geometric parameters, as the flow field is shaped primarily by the hull form rather than propulsion effects. This understanding extends existing hydrodynamic frameworks by characterizing these unique mechanisms in non-powered scenarios.

Moreover, the study elucidates the differential impact of bow geometries on sediment resuspension. Raked bow designs were found to significantly mitigate sediment disturbance compared to blunt bows. This is attributed to the streamlined flow facilitated by raked bows, which reduces shear stresses and limits sediment mobilization. The negative coefficient for the interaction between the Froude number and object type further accentuates the efficacy of raked bows in moderating the effects of hydrodynamic forces on sediment dynamics.

Overall, this study provides a quantitative framework for predicting sediment resuspension based on specific floating object characteristics (e.g., bow shape, dimensions) and operational parameters (e.g., towing speed, clearance height). The insights gleaned are instrumental for the design and operational planning of floating structures, enabling stakeholders to implement strategies that balance operational efficiency with environmental conservation.

6. Conclusions

This study investigated the hydrodynamic and morphological effects caused by non-powered floating objects moving over flat seabeds using computational fluid dynamics (CFD) simulations across 96 different scenarios. These scenarios systematically varied towing speed, squat ratio, towing duration, and bow shapes to elucidate their collective impact on sediment resuspension.

The findings indicate that the towing speed (with Froude number) and squat ratio are the most critical parameters influencing sediment resuspension. Higher towing speeds significantly increased sediment resuspension due to increased flow velocities and shear stresses, while greater clearance heights reduced these effects. The geometry of the floating object also played a significant role; increasing the width amplified sediment resuspension, whereas increasing the length mitigated it. The bow shape affected the amount of sediment resuspension, with blunt bows causing higher sediment disturbance than raked bows.

The multivariate polynomial regression model developed provides a reliable tool for predicting sediment resuspension based on key parameters, with an R-squared value of 0.9647. The model's effectiveness in capturing the complex interactions between variables emphasizes its potential utility in aiding the design and operational planning of floating objects.

These findings bear significant implications for the design and operational planning of floating structures in environmentally sensitive marine ecosystems. By optimizing towing speeds, adjusting squat ratios, and selecting appropriate bow geometries, engineers and designers can effectively mitigate sediment resuspension, thereby minimizing the ecological footprint of maritime activities.

Future research endeavors should aim to expand the dataset to encompass a broader array of operational scenarios and environmental conditions, thereby enhancing the model's generalizability and robustness. Additionally, incorporating supplementary environmental variables and validating the model against empirical field data will bolster its predictive accuracy and applicability. Such advancements will facilitate the development of sustainable maritime practices that harmoniously balance operational efficiency with environmental stewardship, ensuring the preservation of ecological integrity in marine environments.

Author Contributions: Conceptualization, N.G., O.B., M.S.K. and E.İ.; methodology, N.G. and O.B.; software, O.B.; investigation, N.G. and O.B.; resources, N.G., O.B., M.S.K. and E.İ.; writing—original draft preparation, N.G. and O.B.; writing—review and editing, N.G., O.B., M.S.K. and E.İ.; visualization, O.B.; supervision, N.G., M.S.K. and E.İ. All authors have read and agreed to the published version of the manuscript.

Funding: This work was supported by Balikesir University Research Grant No: 2019/021.

Institutional Review Board Statement: Not applicable.

Informed Consent Statement: Not applicable.

Data Availability Statement: The original contributions presented in this study are included in the article. Further inquiries can be directed to the corresponding author.

Conflicts of Interest: The authors declare no conflicts of interest.

References

1. Ravens, T.M. Sediment Resuspension in Boston Harbor. Ph.D. Thesis, Massachusetts Institute of Technology, Cambridge, MA, USA, 1997.
2. Maynord, S.T. *Physical Forces Near Commercial Tows*; Environmental Report 19; U.S. Army Corps of Engineers: Vicksburg, MS, USA, 2000.
3. Parchure, T.M.; McAnally, W.H.; Teeter, A.M. Desktop method for estimating vessel-induced sediment suspension. *J. Hydraul. Eng.* **2001**, *127*, 577–587. [CrossRef]
4. Bauer, B.O.; Lorang, M.S.; Sherman, D.J. Estimating boat-wake-induced levee erosion using sediment suspension measurements. *J. Waterw. Port Coast. Ocean Eng.* **2002**, *128*, 152–162. [CrossRef]
5. McConchie, J.A.; Toleman, I.E.J. Boat wakes as a cause of riverbank erosion: A case study from the Waikato River, New Zealand. *J. Hydrol. N. Z.* **2003**, *42*, 163–179.
6. Houser, C. Sediment resuspension by vessel-generated waves along the Savannah River, Georgia. *J. Waterw. Port Coast. Ocean Eng.* **2011**, *137*, 246–257. [CrossRef]
7. Eriksson, B.K.; Sandström, A.; Isæus, M.; Schreiber, H.; Karås, P. Effects of boating activities on aquatic vegetation in the Stockholm archipelago, Baltic Sea. *Estuar. Coast. Shelf Sci.* **2004**, *61*, 339–349. [CrossRef]
8. Rapaglia, J.; Zaggia, L.; Ricklefs, K.; Gelinas, M.; Bokuniewicz, H. Characteristics of ships' depression waves and associated sediment resuspension in Venice Lagoon, Italy. *J. Mar. Syst.* **2011**, *85*, 45–56. [CrossRef]
9. Zaggia, L.; Lorenzetti, G.; Manfé, G.; Scarpa, G.M.; Molinaroli, E.; Parnell, K.E.; Rapaglia, J.P.; Gionta, M.; Soomere, T. Fast shoreline erosion induced by ship wakes in a coastal lagoon: Field evidence and remote sensing analysis. *PLoS ONE* **2017**, *12*, e0187210. [CrossRef] [PubMed]
10. Duró, G.; Crosato, A.; Kleinhans, M.G.; Roelvink, D.; Uijttewaal, W.S.J. Bank erosion processes in regulated navigable rivers. *J. Geophys. Res. Earth Surf.* **2020**, *125*, e2019JF005438. [CrossRef]
11. Mao, L.; Chen, Y. Investigation of ship-induced hydrodynamics and sediment suspension in a heavy shipping traffic waterway. *J. Mar. Sci. Eng.* **2020**, *8*, 424. [CrossRef]
12. Ji, S.; Ouahsine, A.; Smaoui, H.; Sergent, P. 3D numerical modeling of sediment resuspension induced by the compounding effects of ship-generated waves and the ship propeller. *J. Eng. Mech.* **2014**, *140*, 04014034. [CrossRef]
13. Ji, S.; Ouahsine, A.; Smaoui, H.; Sergent, P. 3D modeling of sediment movement by ships-generated wakes in confined shipping channel. *Int. J. Sediment Res.* **2014**, *29*, 49–58. [CrossRef]
14. Du, J.; Wong, J.; Li, G. Ship-induced sediment suspension in the Changjiang Estuary. *J. Coastal Res.* **2014**, *70*, 167–172. [CrossRef]
15. Robijns, T. Flow Beneath Inland Navigation Vessels. Master's Thesis, Delft University of Technology, Delft, The Netherlands, 2014.

16. Schroevers, M.; Berends, K.D.; Vermaas, T.; Verheij, H.J. Measuring ship-induced currents in a canal. In Proceedings of the 2015 IEEE/OES 11th Current, Waves and Turbulence Measurement (CWTM), St. Petersburg, FL, USA, 2–6 March 2015; pp. 2–7. [CrossRef]
17. *FLOW-3D® HYDRO Version 1.0 Users Manual. FLOW-3D [Computer Software]*, Flow Science, Inc.: Santa Fe, NM, USA, 2020.
18. Yakhot, V.; Smith, L.M. The renormalization group, the ε-expansion and derivation of turbulence models. *J. Sci. Comput.* **1992**, *7*, 35–61. [CrossRef]
19. Soulsby, R. Chapter 9: Bedload transport. In *Dynamics of Marine Sand*; Thomas Telford Publications: London, UK, 1997.
20. Rijn, V.L. Sediment transport, Part I: Bed load transport. *J. Hydraul. Eng.* **1984**, *110*, 1431–1456. [CrossRef]
21. Hirt, C.W.; Nichols, B.D. Volume of fluid (VOF) method for the dynamics of free boundaries. *J. Comput. Phys.* **1981**, *39*, 201–225. [CrossRef]

Disclaimer/Publisher's Note: The statements, opinions and data contained in all publications are solely those of the individual author(s) and contributor(s) and not of MDPI and/or the editor(s). MDPI and/or the editor(s) disclaim responsibility for any injury to people or property resulting from any ideas, methods, instructions or products referred to in the content.